Supplementary Information (SI) for Energy & Environmental Science.

Identifying the role of Zn self-dissolution in the anode corrosion process in Zn-ion batteries

Yi Yuan[1,2]*, Zixuan Li[2], Rongyu Deng[1,3], Shengda D. Pu[2], Marc Walker[1], Mingzhi Cai[2], Feixiang Wu[3], Peter G. Bruce[2,4], Alex W. Robertson[1]*

[1]Department of Physics, University of Warwick, Coventry CV4 7AL, UK

[2]Department of Materials, University of Oxford, Parks Road, Oxford OX1 3PH, UK

[3] National Engineering Research Center of Advanced Energy Storage Materials, School of Metallurgy and Environment, Central South University, 410083, China

[4]Department of Chemistry, University of Oxford, South Parks Road, Oxford OX1 3QZ, UK

* yi.yuan1@warwick.ac.uk ; alex.w.robertson@warwick.ac.uk

Experimental

Chemicals and materials

All chemicals were used directly without any further treatment. 2 M $ZnSO_4$ electrolytes were purchased from Merck Life Science UK Limited, and 1 M $ZnSO_4$ electrolytes were prepared by diluting the 2 M electrolytes. Zinc acetate dihydrate [$Zn(CH_3CO_2)_2{\cdot}2H_2O$, $Zn(OAc)_2$], zinc trifluoromethanesulfonate [$Zn(OTf)_2$], V_2O_5, Zn foil, Ti foil, Cu foil and glass fibre were purchased from Sigma Aldrich. Celgard 3501 was purchased from Celgard, LLC. LIR 2032-coin cell components were purchased from MTI Corporation.

Setup for in situ TEM characterisation

The in situ liquid cell TEM holder (Poseidon 510) and chips (EPB-55DNF and ECT-15WR) used in this work are from Protochips Ltd. The liquid cell holder tip is composed of two silicon chips with electron transparent SiN_x windows, one of which is patterned with platinum (Pt) electrodes. The electrolyte was injected into the holder tip by a syringe pump at a flow rate of 300 µl/h during system purging and at a flow rate of 120 µl/h during TEM imaging.

A Gamry reference 600 was used for galvanotactic measurements. The applied currents in the in situ TEM experiments were 7.5 nA, 12 nA, 15 nA and 30 nA respectively, and the current densities were calculated from the electrode areas of the electrodes patterned on the chips (around 150 μm^2 for in situ experiments and around 300 μm^2 for ex situ experiments). The TEM imaging was carried out with a JEOL JEM-2100 operated at 200 kV, with a 70 µm condenser aperture inserted and a spot size of 3 set up to minimize the beam damage. The beam current was calibrated by a Faraday cup before experiment, and 2 nA was measured under this condition, corresponding to a dose rate of 4 electrons $Å^{-2}$ s^{-1}.

For the additional ex situ studies, the liquid cell setup was assembled using chips with a broader Pt working electrode with a surface area of 300 μm^2, and 1 M $ZnSO_4$ electrolyte was injected into the holder tip at a flow rate of 120 µl/h. Zn was deposited onto the Pt substrate at a current density of 50 mA/cm^2 with a capacity of 1 mAh/cm^2. Afterward, the liquid cell setup was dismantled carefully and the chip with Pt electrode was then immersed in the 1 M electrolyte in a vial for 40 hours.

Electrochemical tests

All coin cells were assembled with a volume of 140 µl electrolyte added and pressed to 1000 psi. The self-supporting V_2O_5 cathode films were prepared by mixing commercial V_2O_5 powder with carbon black and polytetrafluoroethylene in the 6:3:1 mass ratio. Zn||Ti and Zn||Zn coin cells were assembled with two layers of glass fibre. The long-term cycling of coin cells was carried out using a Maccor Series 4000, and all other electrochemical measurements were conducted on a Biologic VMP3 system at a temperature of 30 °C.

Characterisation

Surface morphologies and elemental analysis of Zn electrodes were achieved by a Carl Zeiss Merlin field emission analytical scanning electron microscope coupled with an Oxford instruments Xmax 150 energy dispersive spectrometer. XRD patterns of Zn electrodes were obtained using a Cu source Rigaku diffractometer. The pH values of electrolytes were determined by a Mettler Toledo Seven Excellence pH/mV conductivity meter. The Raman spectra were measured with a Renishaw inVia Qontor spectrometer using a laser of 532 nm. The online mass spectrometry (MS) was conducted by a Thermo Fischer quadrupole mass spectrometer with Ar carrier gas flown at a constant rate of 1 ml min^{-1}.

The x-ray photoelectron spectroscopy (XPS) data were collected by a Kratos Axis Ultra DLD spectrometer which possesses a base pressure below 1×10^{-10} mbar. The samples were illuminated by a monochromated Al Kα x-ray source (hν = 1486.7 eV) and with a low energy electron beam from a charge neutraliser in order to mitigate the build-up of positive charge on the surface during data collection. The core level spectra were recorded using a pass energy of 40 eV (resolution approx. 0.65 eV), from an analysis area of 300 x 700 microns. Sputtering was performed using a monoatomic Ar^+ ion gun at 10 mA emission current, with 4 keV incident ions etching an area on the surface of 4 x 4 mm.

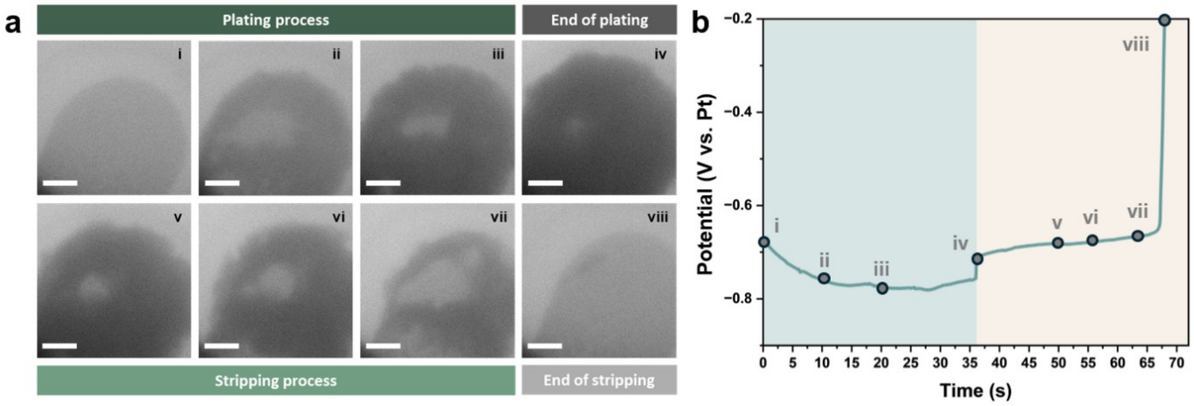

Figure S1. (a) In situ liquid cell TEM imaging of plating and stripping at 10 mA/cm^2 and (b) the corresponding voltage profile. Scale bars are 1 µm.

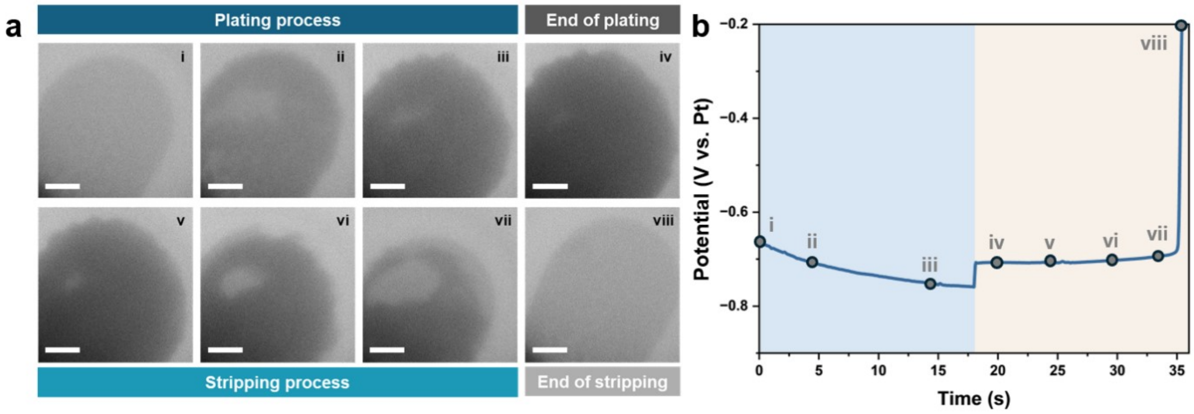

Figure S2. (a) In situ liquid cell TEM imaging of plating and stripping at 20 mA/cm^2 and (b) the corresponding voltage profile. Scale bars are 1 µm.

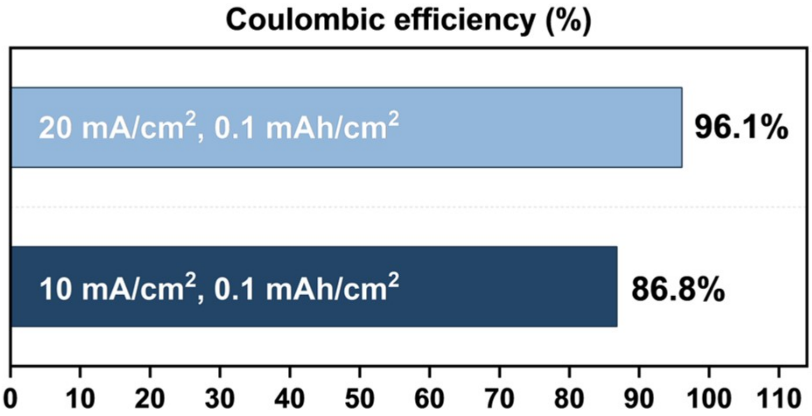

Figure S3. Comparison of the coulombic efficiency at different current densities with the same capacity.

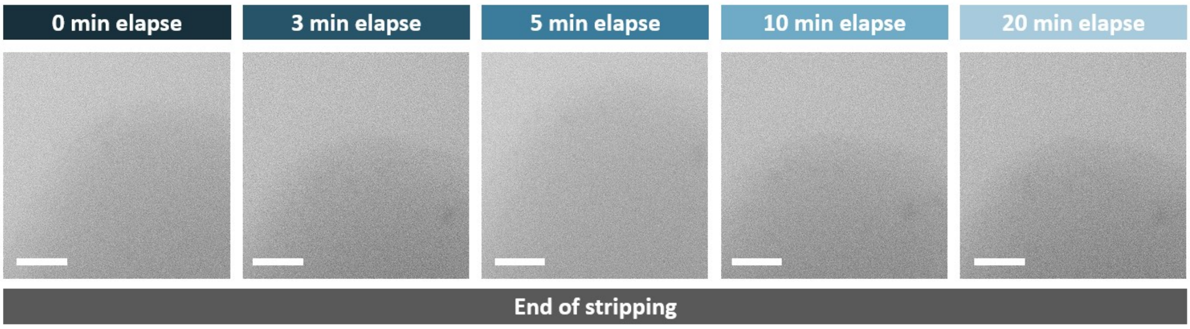

Figure S4. In situ liquid cell TEM images of the end of stripping after rest for different periods of time. Scale bars are 1 µm.

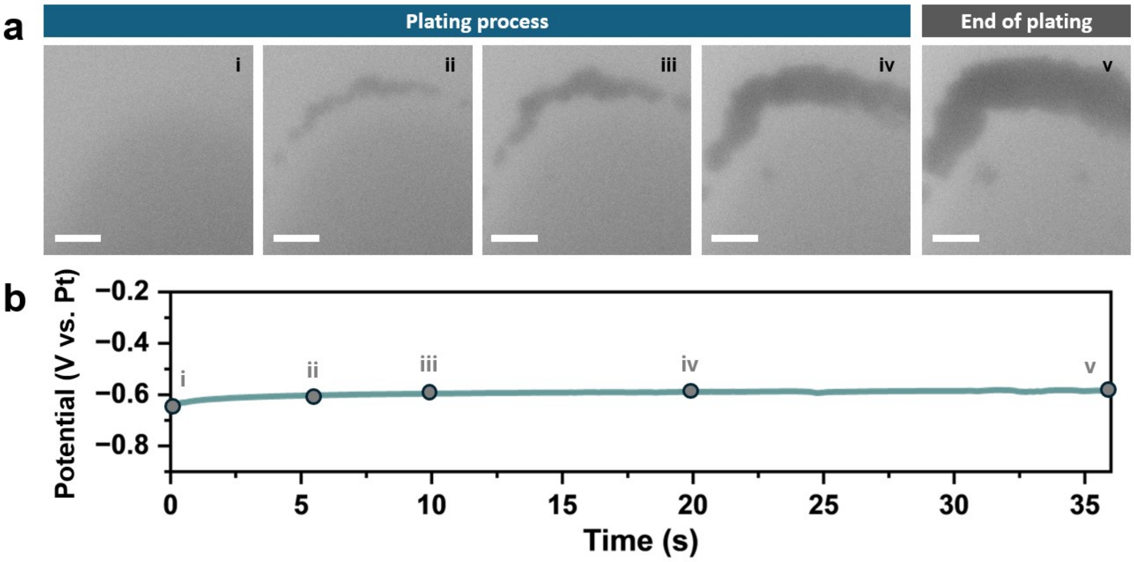

Figure S5. (a) In situ liquid cell TEM imaging of the plating process at a current density of 5 mA/cm^2 and (b) the corresponding voltage profile. Scale bars are 1 µm.

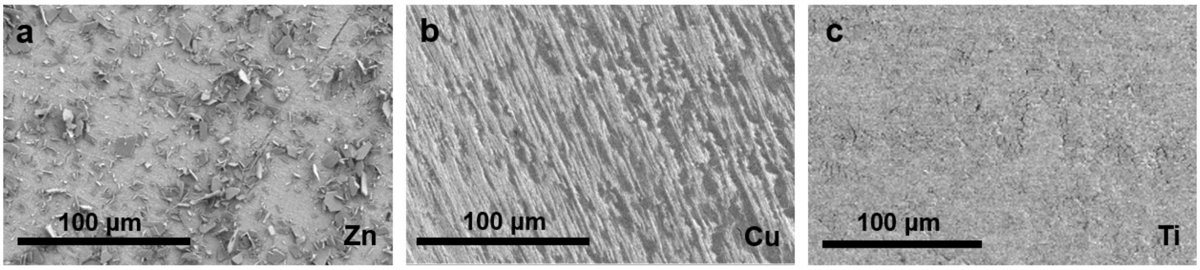

Figure S6. SEM images of (a) the Zn foil, (b) the Cu foil and (c) the Ti foil soaked in vials for 18 hours.

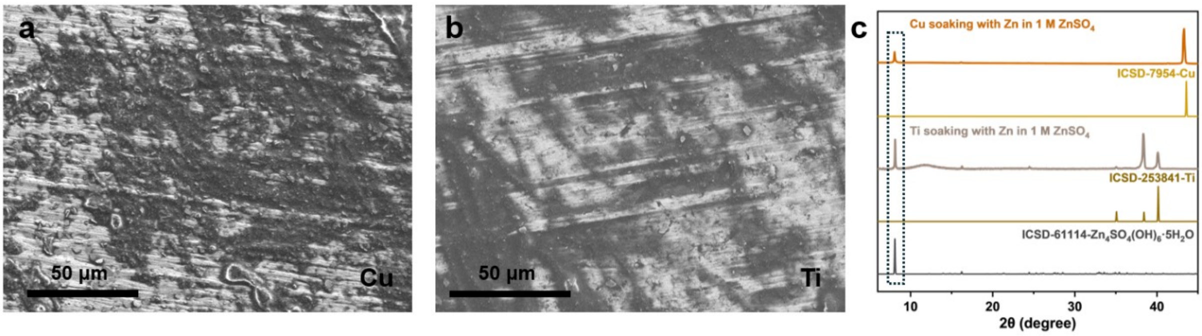

Figure S7. SEM images of (a) the Cu foil and (b) Ti foil soaked together with the Zn foil in the same vial for 18 hours, and (c) their corresponding XRD patterns.

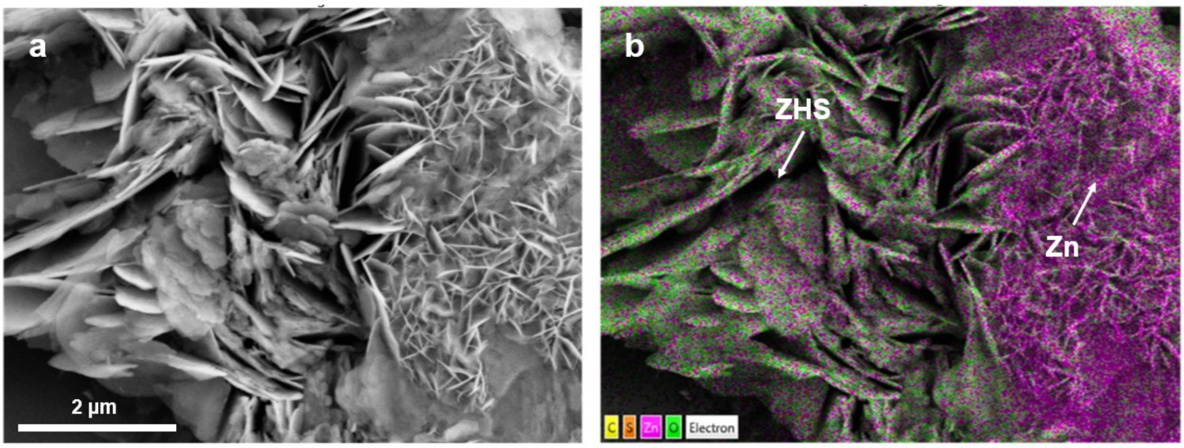

Figure S8. (a) SEM image and (b) EDX mapping of a liquid cell TEM electrode after three plating/stripping cycles at a current density of 20 mA/cm².

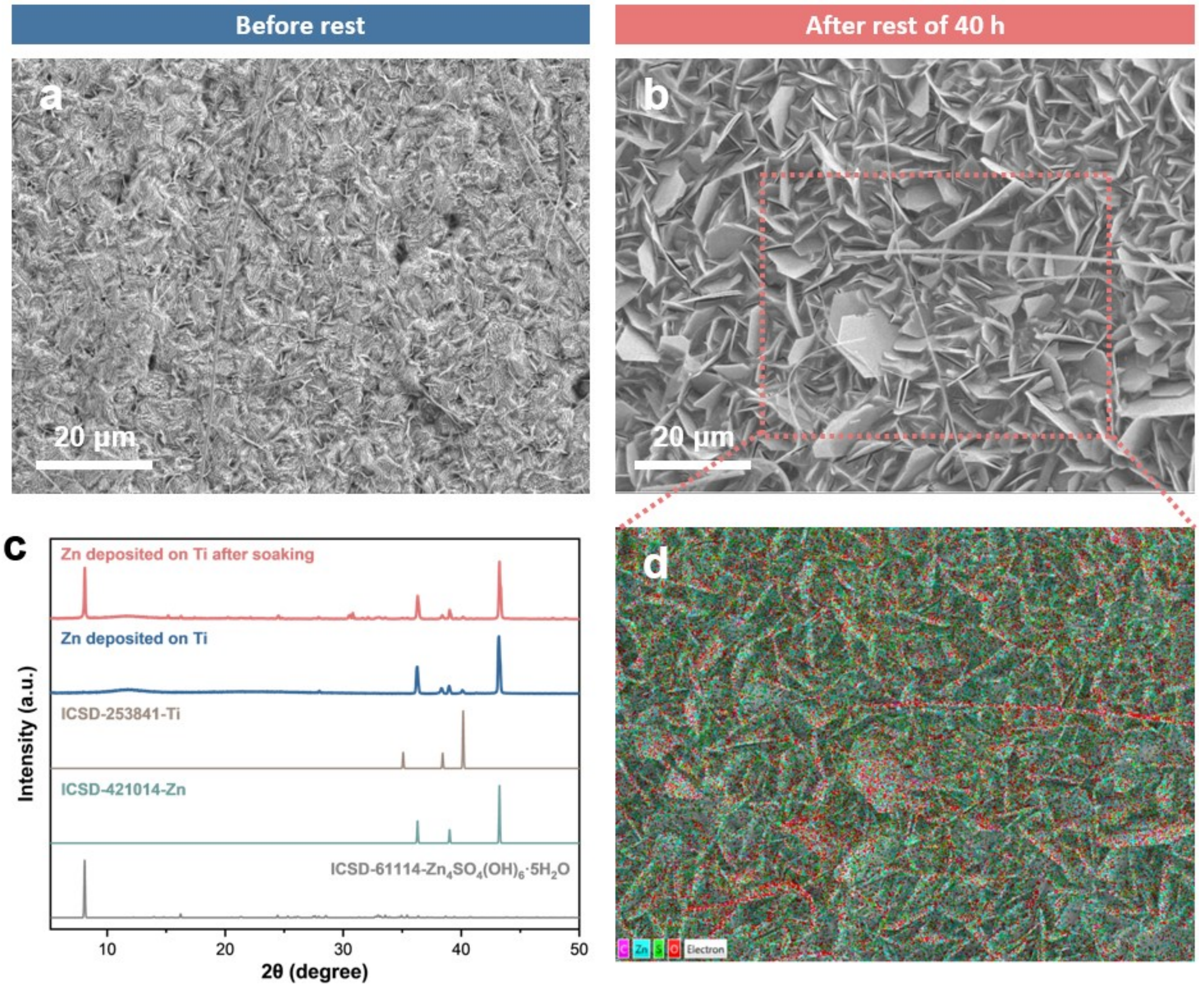

Figure S9. SEM images of the thin Zn film deposited on the Ti foil (a) before and (d) after rest for 40 hours. (c) The corresponding XRD patterns of the Zn film deposited on the Ti foil before and after rest. (d) The EDX mapping of the thin Zn film on the Ti foil after rest.

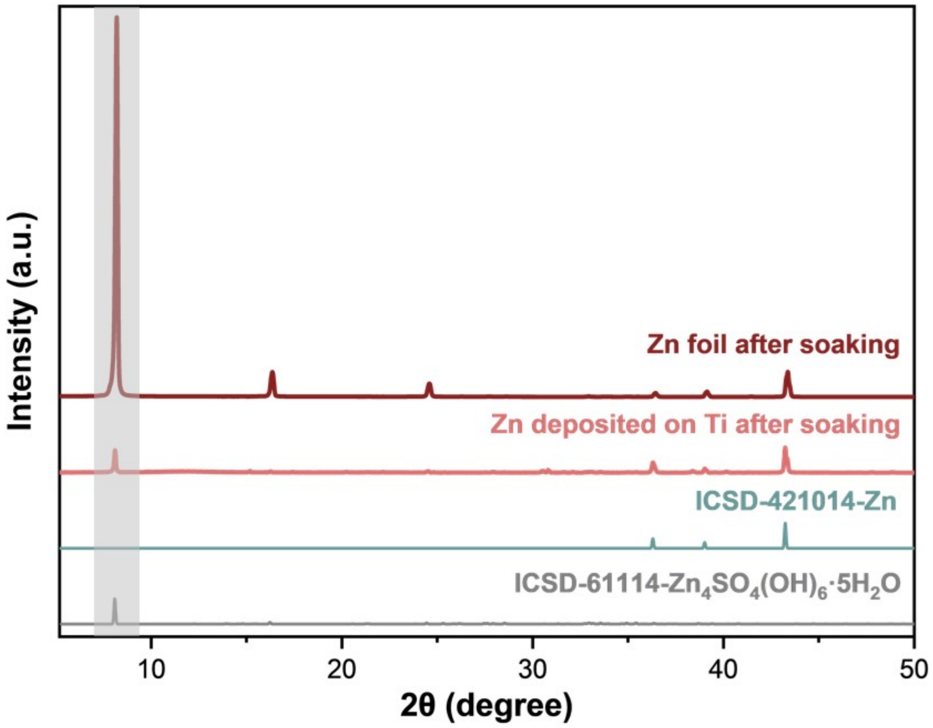

Figure S10. Comparisons of the XRD patterns of the thin Zn film deposited on the Ti foil and the Zn foil after soaking in the $ZnSO_4$ electrolyte in vials for 40 hours, indicating the difference in the amount of ZHS byproducts.

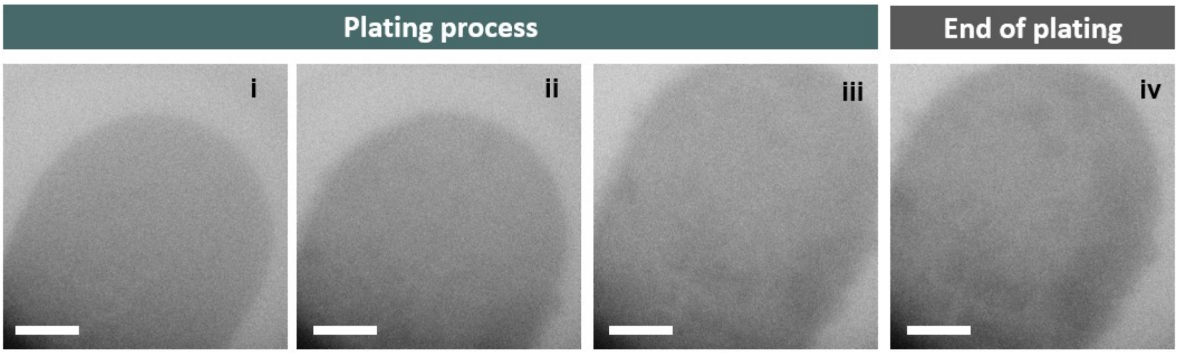

Figure S11. In situ liquid cell TEM imaging of the plating process at a current density of 5 mA/cm^2 in the ZnSO$_4$ electrolyte with Zn(OAc)$_2$. Scale bars are 1 µm.

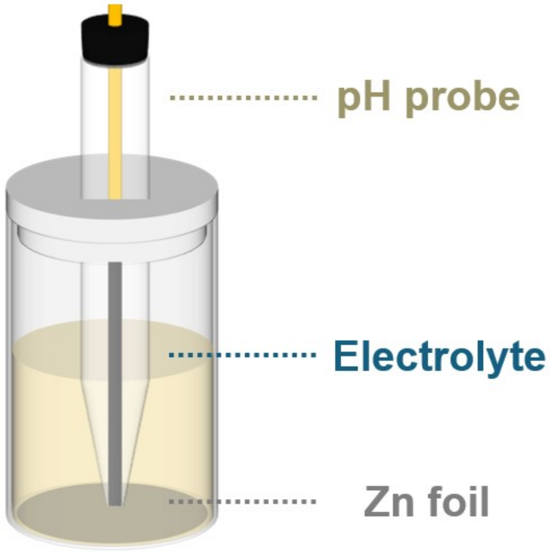

Figure S12. Illustration of the home-made setup for the in situ pH monitoring near the surface of the Zn foil soaked in different electrolytes. Zn foil was placed at the bottom of a vial with 2 ml electrolyte added, with the pH probe fixed to ensure close contact of the tip with the Zn foil surface.

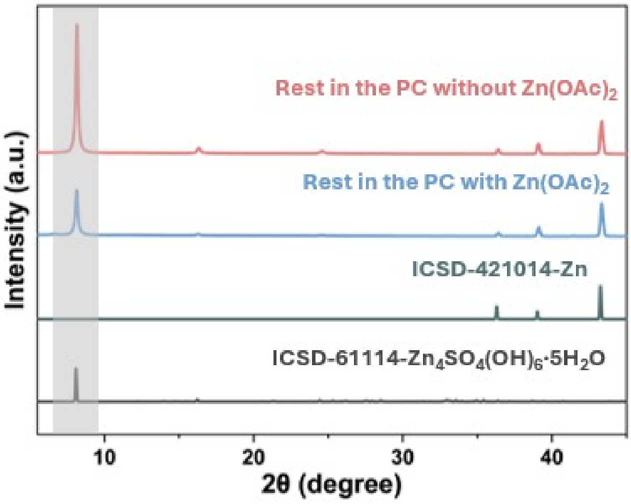

Figure S13. XRD patterns of Zn electrodes after rest in pouch cells with the $ZnSO_4$ electrolyte without and with the addition of $Zn(OAc)_2$.

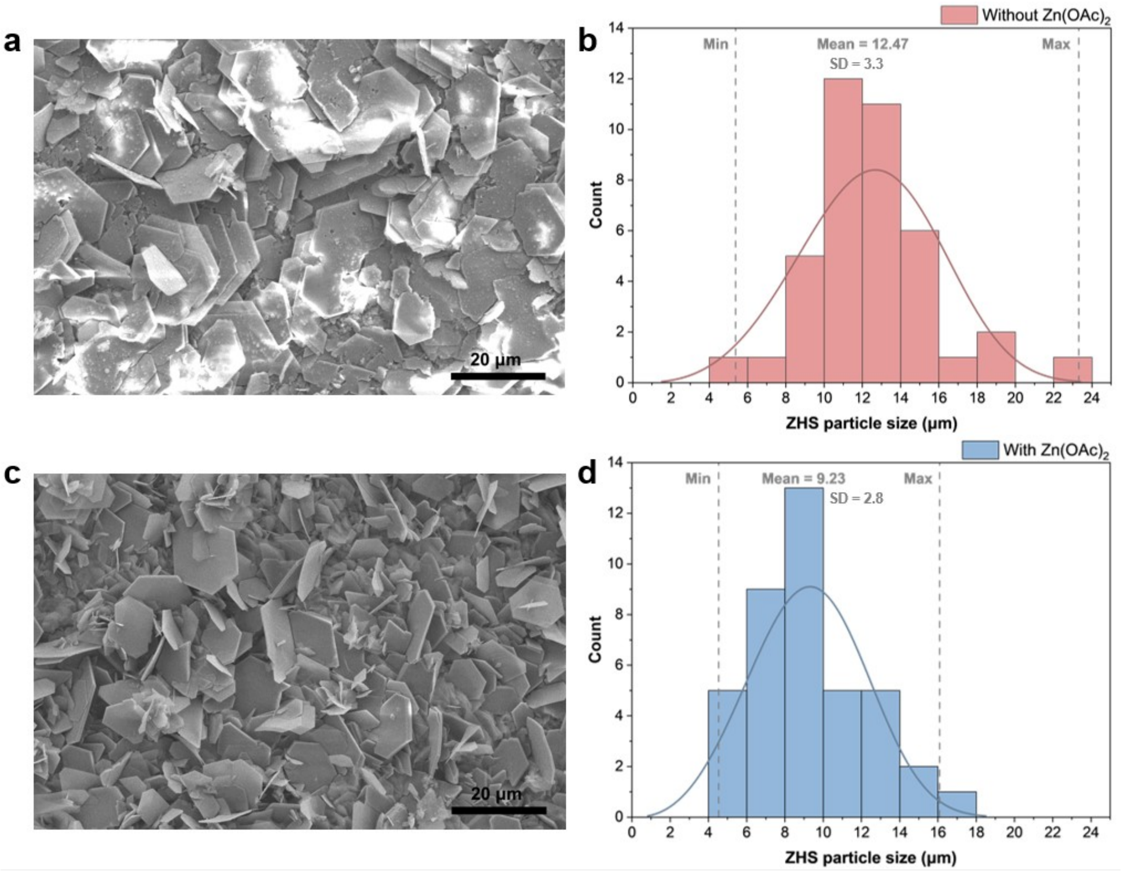

Figure S14. (a, c) The SEM images and (b, d) the particle size distribution of ZHS flakes on the Zn surface after soaking for 40 hours and in the electrolyte without and with $Zn(OAc)_2$.

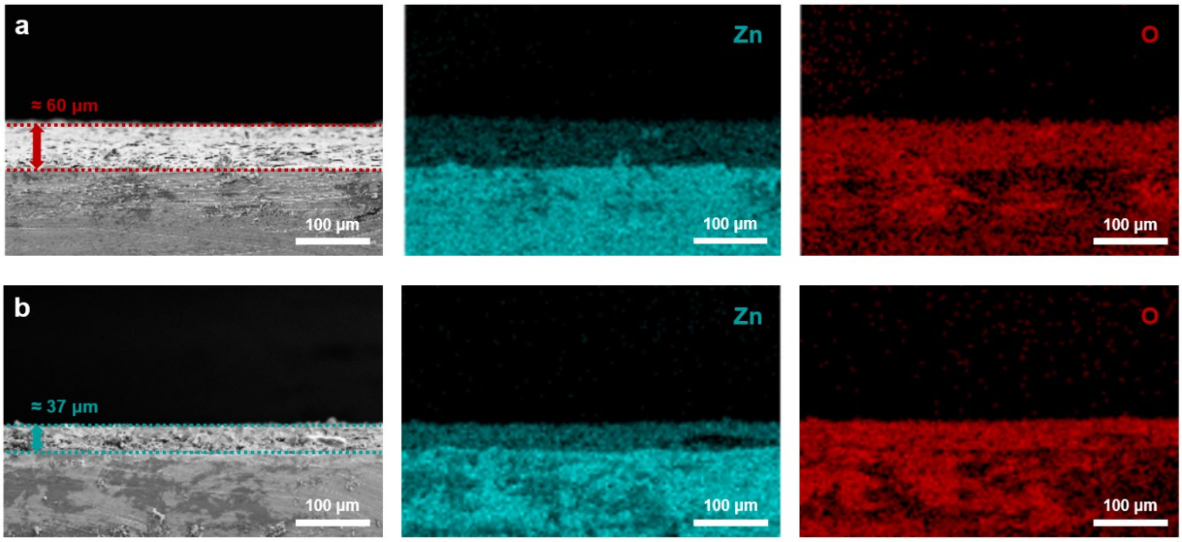

Figure S15. The SEM imaging and EDX mapping results for the cross section of Zn after soaking in the electrolyte (a) without and (b) with $Zn(OAc)_2$ addition.

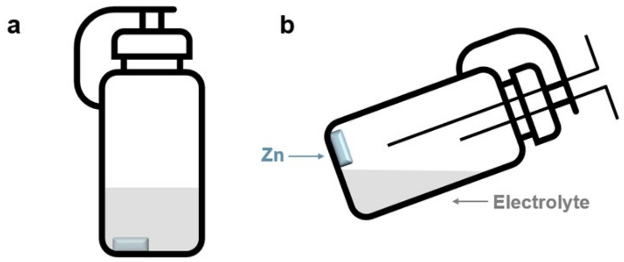

Figure S16. The experimental setup for online MS to quantify the hydrogen evolution during rest.

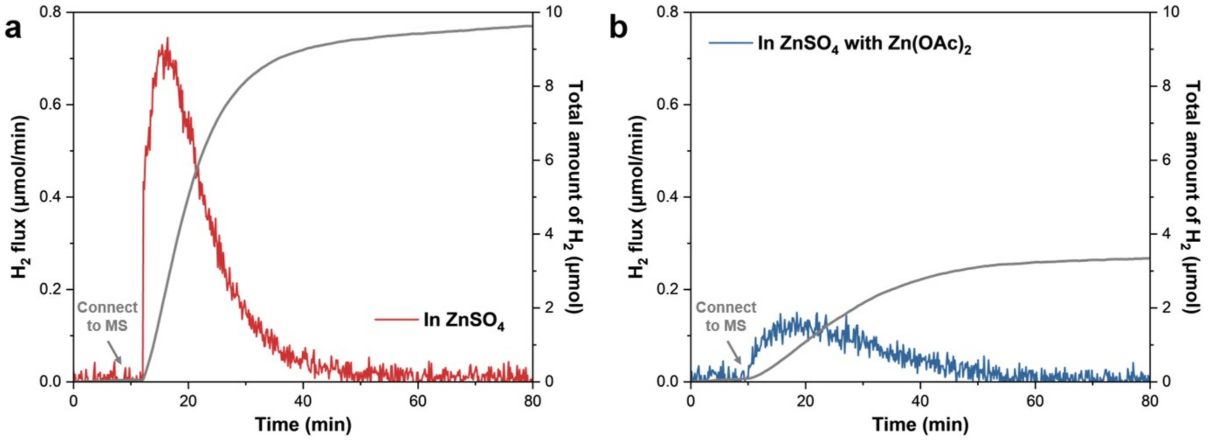

Figure S17. MS profiles of hydrogen evolution (a) in the $ZnSO_4$ electrolyte and (b) in the $ZnSO_4$ electrolyte with $Zn(OAc)_2$ after soaking Zn foils in vials.

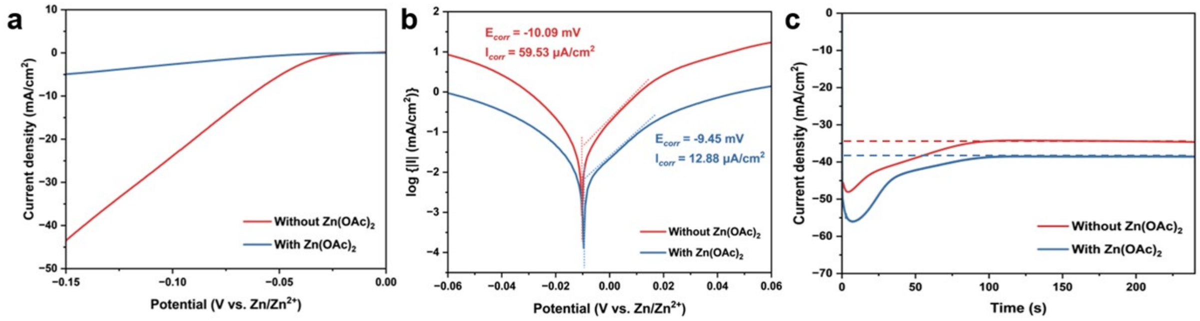

Figure S18. (a) The LSV curves tested at a scan rate of 10 mV/s, (b) the Tafel plots, and (c) the chronoamperometry curves tested at a fixed potential of -150 mV in the $ZnSO_4$ electrolyte without and with the $Zn(OAc)_2$ addition.

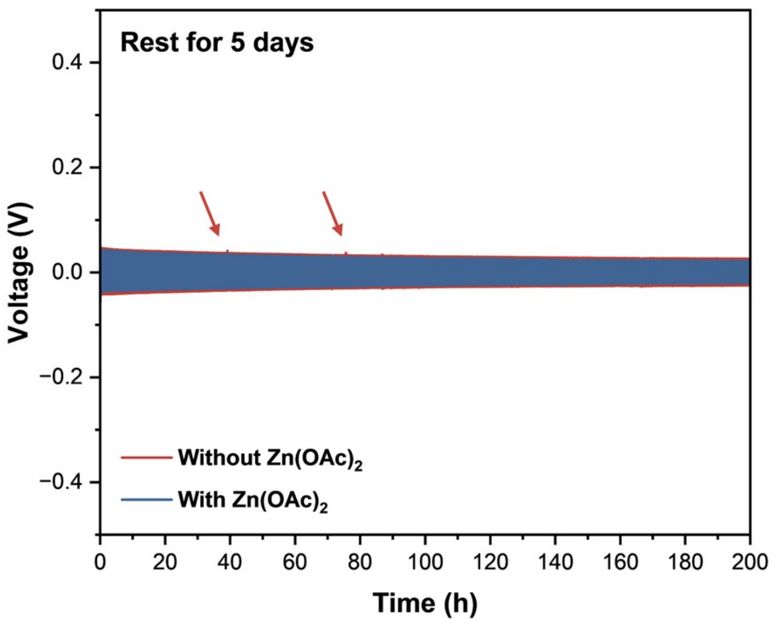

Figure S19. The voltage profiles of Zn||Zn symmetric coin cells after rest for 5 days using the $ZnSO_4$ electrolyte without and with the $Zn(OAc)_2$ addition.

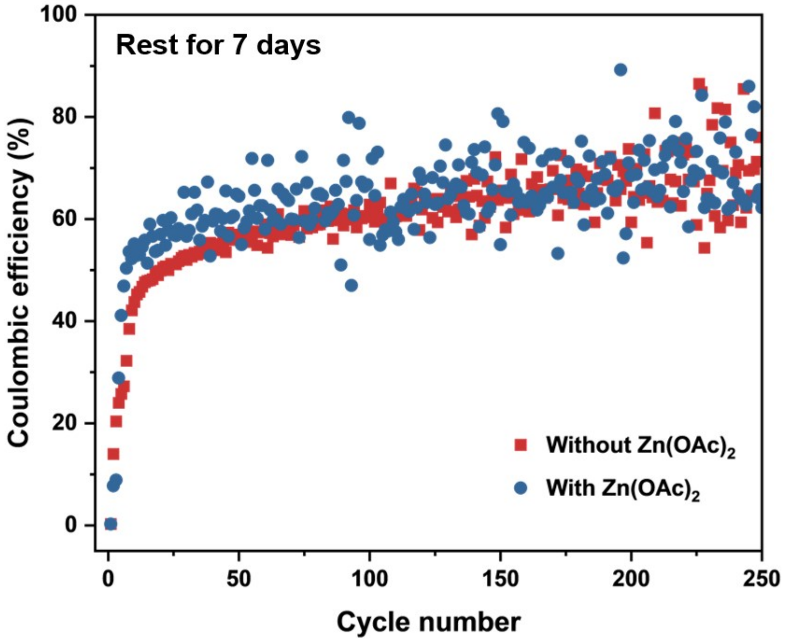

Figure S20. The coulombic efficiency of Zn||Ti coin cells after resting for 7 days using the electrolyte of $ZnSO_4$ without and with $Zn(OAc)_2$ addition.

The Zn||Ti coin cells were cycled at a current density of 10 mA/cm^2 after resting for 7 days. A slightly higher coulombic efficiency was achieved in the cell with $Zn(OAc)_2$ added, indicating mitigated side reactions during cycling.

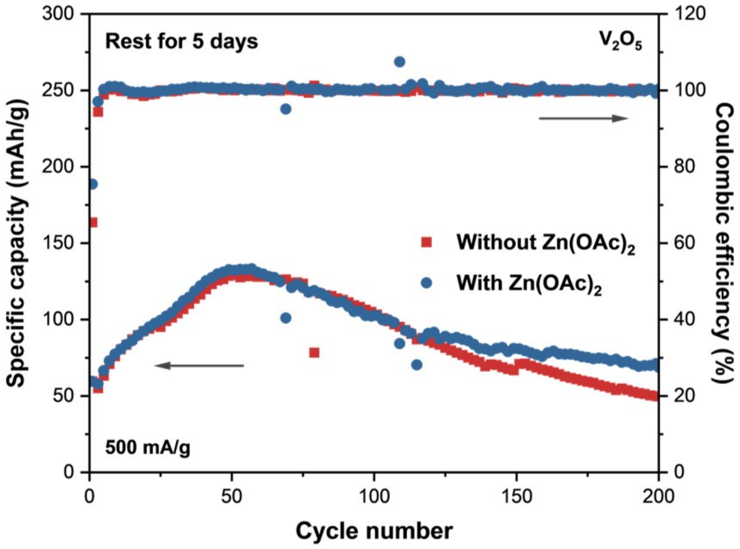

Figure S21. The cycling performance of Zn||V_2O_5 coin cells using the electrolyte of $ZnSO_4$ without and with $Zn(OAc)_2$ addition.

The cycling performances of full cells with V_2O_5 as the cathode using the electrolyte with and without $Zn(OAc)_2$ after resting for 5 days were compared. The induction of $Zn(OAc)_2$ to the electrolyte barely had impact on the capacity and coulombic efficiency of the Zn||V_2O_5 cell during initial cycling. However, a slight increase in capacity was found after 100 cycles.

It should be noted that the pH of electrolytes not only affects the Zn metal anode but also plays a crucial role in determining cathode performance [1]. Moreover, the anionic component of Zn salts also influences cathode behaviour and capacity storage mechanisms [2]. As a result, evaluating the impact of pH adjustment by adding $Zn(OAc)_2$ on Zn self-corrosion solely by comparing full cell performance after rest is inherently complex. However, this further highlights the importance of considering how different electrolyte engineering strategies affect pH and, in turn, the overall battery performance.

Table 1. Summary of the reactions during rest and cycling

HER	$2H^+ + 2e^- \rightarrow H_2$✁
Zn deposition/stripping	$Zn^{2+} + 2e^- \rightarrow Zn$
	$Zn - 2e^- \rightarrow Zn^{2+}$
Zn self-dissolution	$Zn + 2H^+ \rightarrow Zn^{2+} + H_2$✁
Precipitation of ZHS	$4Zn^{2+} + 6OH^- + SO_4^{2-} + xH_2O \rightarrow Zn_4(OH)_6SO_4 \cdot xH_2O$
pH adjustment by acetate anions	$CH_3COO^- + H^+ \rightarrow CH_3COOH$ (Increase in the initial pH)
	$CH_3COOH + OH^- \rightarrow CH_3COO^- + H_2O$ (Buffering effect during cycling)

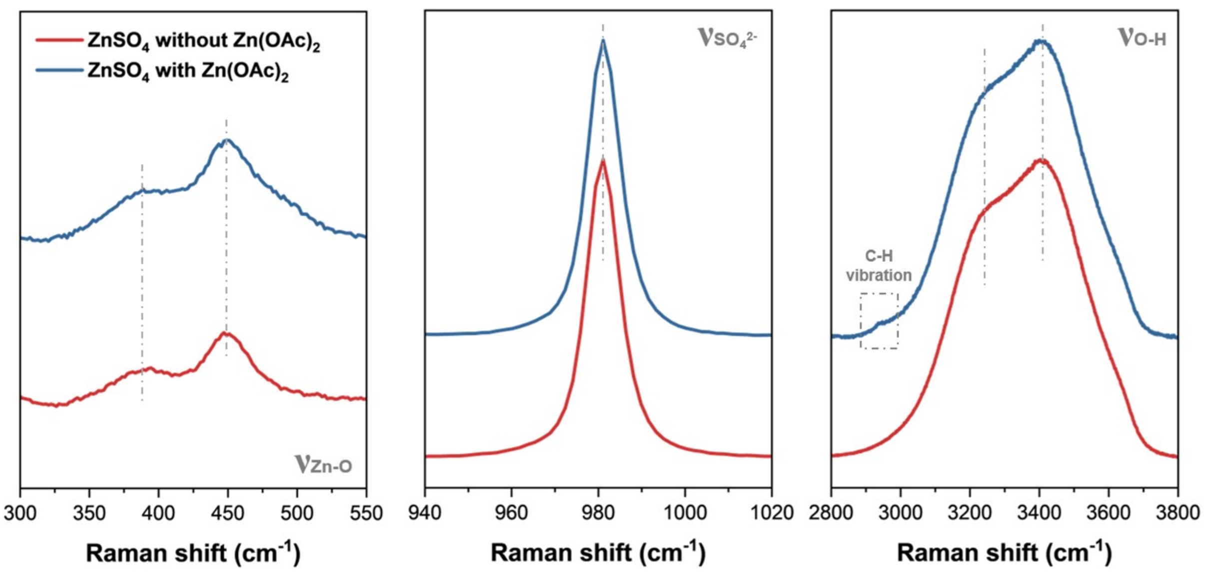

Figure S22. The Raman spectra of the aqueous $ZnSO_4$ electrolyte without and with the addition of $Zn(OAc)_2$, including the $\nu_{Zn\text{-}O}$, ν_{SO42-}, and $\nu_{O\text{-}H}$ stretching vibration.

The peak positions and intensities of the Zn-O, SO_4^{2-}, and O-H stretching bands remained unchanged, indicating that the solvation structure of Zn-hydrated ions and the water network was not altered by the presence of $Zn(OAc)_2$. A small peak emerged at around 2940 cm^{-1} in the spectrum of the electrolyte containing $Zn(OAc)_2$, corresponding to the C-H stretching vibration, which confirms the presence of a small amount of OAc^- anions. However, this minor amount of OAc^- did not cause any noticeable changes to the main solvation structures, as evidenced by the consistency of the Zn-O, SO_4^{2-}, and O-H stretching bands.

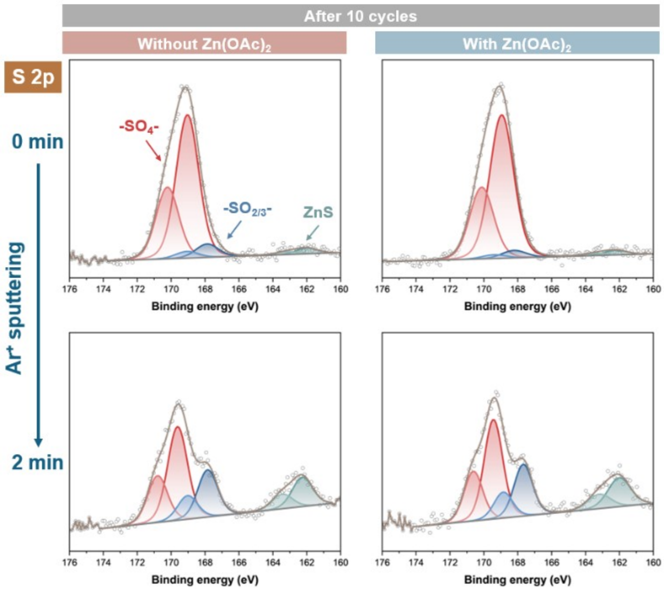

Figure S23. The XPS depth profile for S 2p spectra of the Zn metal anodes after 10 cycles (10 mA/cm^2, 1 mAh/cm^2) in the $ZnSO_4$ electrolyte without and with $Zn(OAc)_2$.

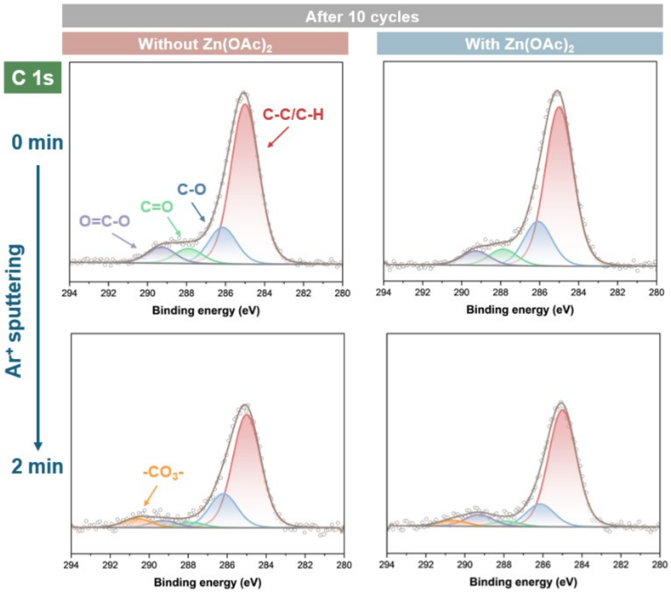

Figure S24. The XPS depth profile for C 1s spectra of the Zn metal anodes after 10 cycles (10 mA/cm^2, 1 mAh/cm^2) in the $ZnSO_4$ electrolyte without and with $Zn(OAc)_2$.

According to the S 2p and C 1s spectra of Zn electrodes after cycling, the elemental composition remained unchanged, indicating that acetate anions do not actively participate in the electrodeposition process. The presence of ZnS and $-SO_2/_3^-$ species in the S 2p spectra suggests the partial decomposition of SO_4^{2-} during cycling.

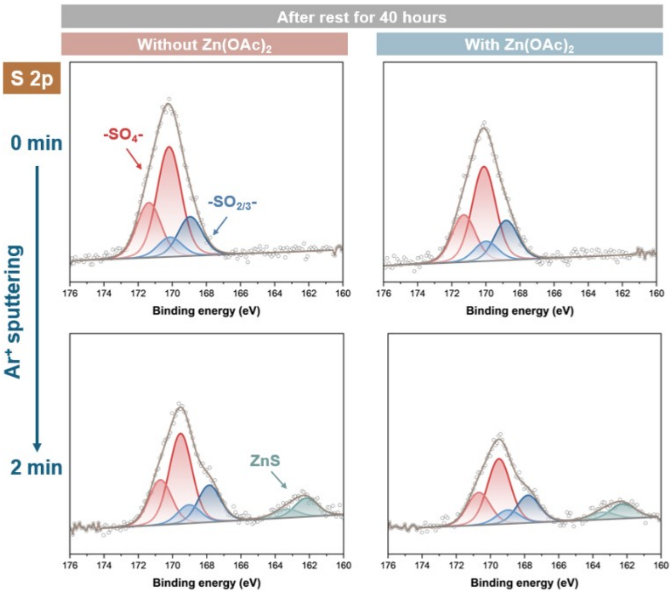

Figure S25. The XPS depth profile for S 2p spectra of the Zn foils after 40-hour rest in the $ZnSO_4$ electrolyte without and with $Zn(OAc)_2$.

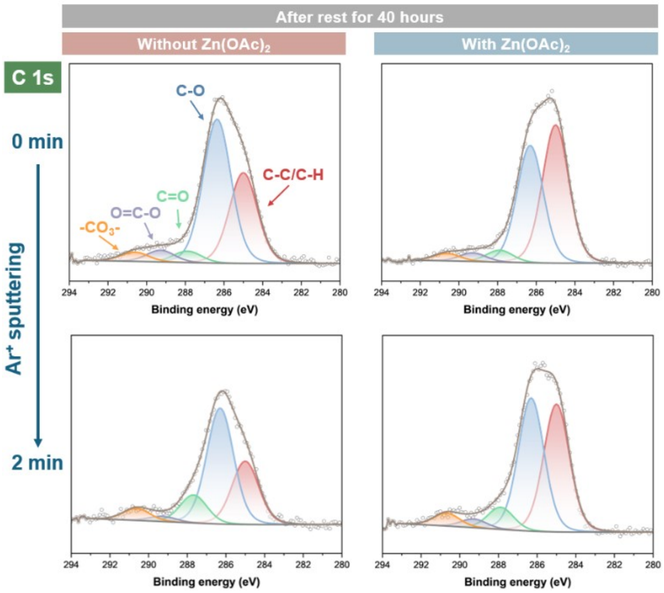

Figure S26. The XPS depth profile for C 1s spectra of the Zn foils after 40-hour rest in the $ZnSO_4$ electrolyte without and with $Zn(OAc)_2$.

After 40 hours of rest, only $-SO_x^-$ peaks appear after sputtering, indicating the accumulation of residual Zn salts or ZHS byproducts on the surface. In the C 1s spectra, the Zn foils show a stronger C signal compared to those after cycling, which may result from long-term exposure to dissolved CO_2 in the aqueous electrolyte, adsorption on the surface, or residual ethanol from the washing process. The Zn foil immersed in the electrolyte containing $Zn(OAc)_2$ exhibits an increased carbon signal, with a higher area ratio of the C-C/C-H bond peak compared to the electrolyte without $Zn(OAc)_2$. This can be attributed to the residual from the acetate species on the Zn surface over long-term immersion.

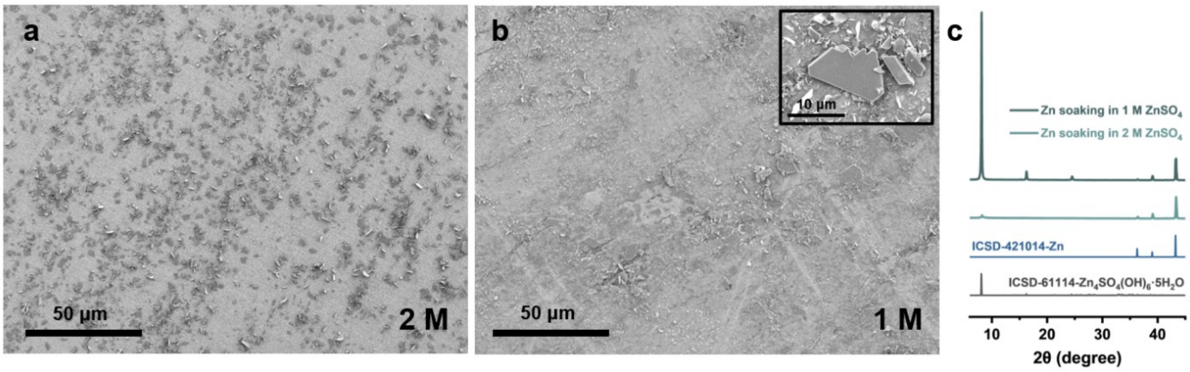

Figure S27. SEM images of Zn foils soaked in (a) the 2 M $ZnSO_4$ electrolyte and (b) the 1 M $ZnSO_4$ electrolyte, and (c) the corresponding XRD patterns.

The corrosion process of Zn in Zn-ion batteries with acidic electrolytes is influenced by more than just the pH value. For example, it is necessary to take the salt concentration of the $ZnSO_4$ electrolyte into account in the study of the self-corrosion process of the Zn anode. Figure S16 shows the SEM images and XRD patterns of Zn foils after resting in vials in $ZnSO_4$ electrolytes of varying concentrations for 18 hours. The Zn foil immersed in the 1 M electrolytes experienced a more severe corrosion issue, as evidenced by a greater presence of ZHS flakes and stronger XRD peaks for ZHS. The 1 M and 2 M $ZnSO_4$ electrolytes share close pH values, which are around 4.46 and 4.21 respectively, according to our measurement. Although the pH of the 2 M $ZnSO_4$ electrolyte is even slightly lower, much fewer ZHS byproducts were observed. It is generally believed that higher concentrations of electrolytes will weaken the interactions between the active Zn metal anode and water molecules [3-5]. Hence, the self-corrosion of Zn could also be alleviated by using electrolytes of high concentrations.

Interestingly, several recent studies have also proposed that the corrosion and hydrogen evolution during cycling can be mitigated by using ultra-low-concentration $ZnSO_4$ electrolytes [6]. This counterintuitive strategy is thought to work because the hydrated species and the sum of Zn^{2+}-solvated water are considered to be responsible for the hydrogen evolution, which can be effectively reduced by lowering the concentration of Zn salt in electrolytes. However, the underlying mechanisms for reduced corrosion during rest in these electrolytes of ultra-low concentrations are still unclear.

From the perspective of pH, $ZnSO_4$ electrolytes of ultra-low concentrations have slightly higher pH values according to previous research [7]. This may have a positive influence on easing Zn self-dissolution, but other factors should also be considered. It should be noted that not only the OH^- concentration, but also the concentrations of other species, including Zn^{2+} and SO_4^{2-} ions, play a crucial role in the precipitation of ZHS. Consequently, it is also reasonable to see the reduced formation of ZHS during battery rest in electrolytes of lower salt concentrations.

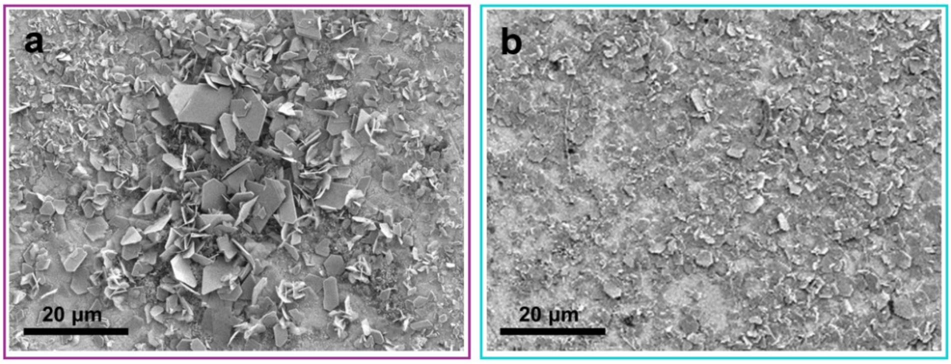

Figure S28. The SEM images of the byproducts forming on the Zn foils (a) soaked in the vial with 1 ml $ZnSO_4$ electrolyte, and (b) sealed in the pouch cell with 140 µl $ZnSO_4$ electrolyte, for 18 hours.

We believe the amount of electrolyte has some effect on the Zn corrosion during rest. To confirm this, we compared the Zn foil surface soaked in the vial with 1 ml $ZnSO_4$ electrolyte, and sealed in the pouch cell with 140 µl electrolyte, for 18 hours. From the comparisons above, it is evident that the amount of electrolyte plays a crucial role in the formation of ZHS. The quantity and particle size of byproducts formed in the vial are larger than those in the pouch cell, where the electrolyte amount and available space are more limited. This suggests that an excess of electrolyte promotes more extensive ZHS formation during the rest period.

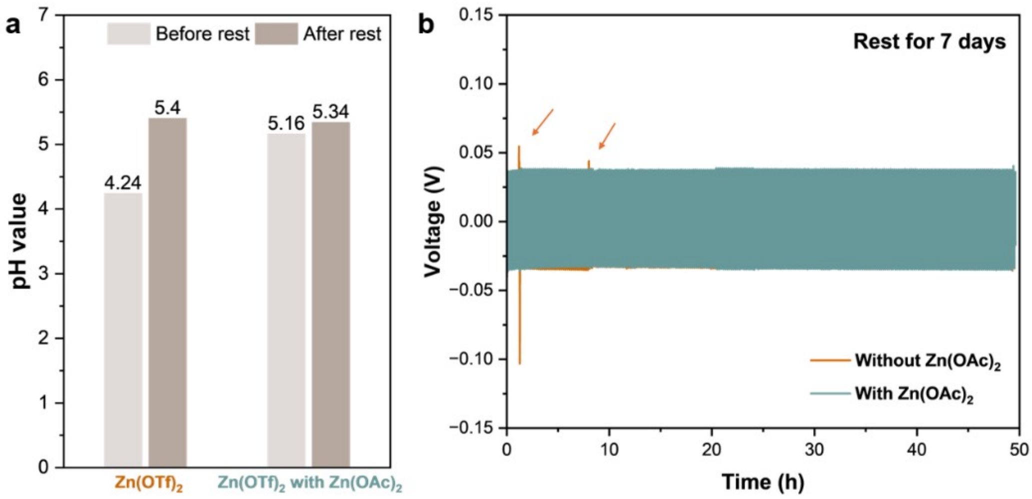

Figure S29. (a) Comparison of pH values near the Zn soaked in the $Zn(OTf)_2$ electrolyte without and with $Zn(OAc)_2$ before and after resting for 20 hours. (b) The voltage profiles of Zn||Zn symmetric coin cells after rest for 7 days using the $Zn(OTf)_2$ electrolyte without and with the $Zn(OAc)_2$ addition.

We also use another commonly used Zn electrolyte, $Zn(OTf)_2$ (zinc trifluoromethanesulfonate), as a demonstration. The pH changes near the Zn metal surface before and after immersion into the 1 M $Zn(OTf)_2$ electrolyte without and with addition of $Zn(OAc)_2$ were tested, and the cycling performance of Zn||Zn symmetric cells after resting for a week were compared. A more pronounced increase in pH was observed in the $Zn(OTf)_2$ electrolyte, accompanied by fluctuations in the voltage profile of the coin cell using pure 1 M $Zn(OTf)_2$ electrolyte (indicated by orange arrows).

Reference

1. Zeng, X. *et al*. Toward a reversible Mn^{4+}/Mn^{2+} redox reaction and dendrite-free Zn anode in near-neutral aqueous Zn/MnO_2 batteries via salt anion chemistry. *Adv. Energy Mater.* **10**, 1904163 (2020).

2. Du, Y. *et al*. Electrolyte salts and additives regulation enables high performance aqueous zinc ion batteries: a mini review. *Small* **18**, 2104640 (2022).

3. Zhang, C. *et al.* A $ZnCl_2$ water-in-salt electrolyte for a reversible Zn metal anode. *Chem. Commun.* **54**, 14097–14099 (2018).

4. Zhang, L. *et al.* $ZnCl_2$ “Water-in-Salt” Electrolyte Transforms the Performance of Vanadium Oxide as a Zn Battery Cathode. *Adv. Funct. Mater.* **29**, 1902653 (2019).

5. Chen, J. *et al*. Challenges and Perspectives of Hydrogen Evolution-free Aqueous Zn-Ion Batteries. *Energy Storage Mater*. **59**, 102767 (2023).

6. Qian, L. *et al.* Ultralow-Salt-Concentration Electrolyte for High-Voltage Aqueous Zn Metal Batteries. *Adv. Funct. Mater.* **33**, 2301118 (2023).

7. Miao, L. *et al.* A Universal Descriptor in Determining H_2 Evolution Activity for Dilute Aqueous Zn Batteries. *Adv. Funct. Mater.* **33**, 2306952 (2023).